Characterization of Induced Current Density During Transcorneal Electrical Stimulation to Promote Neuroprotection in the Degenerating Retina

Ege Iseri, Pragya Kosta, Dimitrios Pollalis, Pei-An Lo, Ben Yi Tew, Stan Louie, Bodour Salhia, Mark Humayun and Gianluca Lazzi

***Abstract*— *Objective:* Transcorneal electrical stimulation (TES) is a promising approach to delay retinal degeneration by inducing extracellular electric field-driven neuroprotective effects within photoreceptors. Although achieving precise electric field control is feasible in vitro, characterizing these fields becomes intricate and largely unexplored in vivo due to uneven distribution in the heterogeneous body. In this paper, we investigate and characterize electric fields within the retina during TES to assess the potential for therapeutic approaches *Methods:* We developed a computational model of a rat's head, enabling us to generate predictive simulations of the voltage and current density induced in the retina. Subsequently, an in vivo experimental setup involving Royal College of Surgeon (RCS) rats was implemented to measure the voltage across the retina using identical electrode configurations as employed in the simulations. *Results:* A stimulation amplitude of 0.2-0.3 mA may be necessary during TES in rats to induce a current density of at least 20 A/m^2 in the retina, which is the lower limit for triggering neuroprotective effects according to culture studies on neural cells. Measurement taken from cadaveric pigs' eyes revealed that a stimulation amplitude of 1 mA is necessary for achieving the same current density. *Conclusion:* The computational modeling approach presented in this study was validated with experimental data and can be leveraged for predictive simulations to optimize the electrode design and stimulation parameters of TES. *Significance:* Once validated, the flexibility and low research cost of computational models are valuable in optimization studies where testing on live subjects is not feasible.**

***Index Terms*—bioelectromagnetics, computational modeling, electrophysiology, retinal degeneration, neuroprotection, transcorneal electrical stimulation**

This research was based upon work supported by grants from the National Science Foundation under Grant Nos 1933394, 2121164; and supported/partially supported by the USC Center for Neuronal Longevity (#PG1033624); Unrestricted Grant to the Department of Ophthalmology from Research to Prevent Blindness, New York, NY; Dr. Allen and Charlotte Ginsburg Institute for Biomedical Therapeutics; Dennis and Michele Slivinski; The USC Roski Eye Institute; Dr. Ramani Nathan; and The Retina Research Foundation's Gertrude D. Pyron Award. No funding sponsors were involved in the study design, collection, analysis, interpretation of data, writing of report, or decision to submit the article for publication.

E. Iseri is with the Department of Biomedical Engineering and the Institute for Technology and Medical Systems at the University of Southern California, USA. D. Pollalis, P. Lo and M. Humayun are with the Ginsburg Institute for Biomedical Therapeutics, Roski Eye Institute, Department of Ophthalmology at the University of Southern California, USA. P. Kosta was with the Institute for Technology and Medical Systems at the University of Southern California, USA. B.Y. Tew and B. Salhia are with the Department of Translational Genomics, Keck School of Medicine at the University of Southern California. S. Louie is with Ginsburg Institute for Biomedical Therapeutics and Department of Clinical Pharmacy at the University of Southern California, USA. G. Lazzi is with the Institute for Technology and Medical Systems, the Department of Ophthalmology, and the Department of Electrical and Computer Engineering at the University of Southern California, Los Angeles, CA, USA (correspondence e-mail: lazzi@usc.edu).

I. INTRODUCTION

Neuronal loss is a defining characteristic of retinal dystrophies, encompassing conditions such as retinitis pigmentosa, age-related macular degeneration (AMD), and primary open-angle glaucoma [1-3]. Advances in ophthalmology have introduced innovative strategies to counteract the debilitating impact of retinal degeneration like gene therapy [4], cell therapy [5-7] and retinal prostheses [8]. Among these pioneering approaches, TES of the retina has emerged as a promising strategy for slowing down the progression of retinal degeneration. Evidence from animal and clinical studies suggests that electrical stimulation possesses therapeutic potential for retinal neurons and offers potential avenues for managing neurodegenerative conditions such as retinitis pigmentosa [9, 10]. The capacity of electrical stimulation to enhance cell survival and activity was demonstrated on various retinal cell types. Exposing cell cultures in vitro to electrical fields stimulated the expression of neurotrophic factors by Schwann cells [11], induced Muller Cell proliferation and production of neurotrophic factors [12], improved photoreceptor survival in rodent specimens with light-induced damage or inherited degeneration [13-15], rescued or increased survival rate of injured retinal ganglion cells [16-18]. TES has showcased its potential in preserving the integrity of the outer nuclear layer and enhancing the functionality of electroretinography following a six-week stimulation period in live rats [19]. Electrical stimulation can contribute to neuronal preservation, primarily through the modulation of neurotrophic factors after TES sessions [15, 20, 21]. These studies collectively suggest that electrical stimulation holds promise in promoting neuroprotection by enhancing cell survival, reducing oxidative stress and inflammation, and increasing expression of neurotrophic factors.

Despite the promising foundations of EF-induced neuroprotection in cell culture and animal studies, the long-term TES clinical trials have yielded partial success, suggesting the need for methodological optimization. Improvements in the retinal function and preservation of the visual field of RP patients have been observed in some trials utilizing either the OkuStim system or DTL skin patch electrodes [22-25], whereas no significant difference was observed between control and stimulation eyes in other trials also using the OkuStim system [26, 27]. Another study found improvement in the metabolic function of the retina in terms of oxygen consumption but no significant change in the retinal vessel diameters following TES in RP patients [28]. Due to the mixed outcomes of these trials, the relationship between electrode design, waveform parameters and stimulation duration for effective therapeutics is still not standardized. One of the limiting factors in assessing the success of the electrical stimulation therapies so far is the metric used for characterizing the stimulator setup between different trials. The effectiveness of neuromodulation and TES trials on animal models and humans is commonly gauged with respect to the stimulation amplitude in a current-controlled system, which ranges from 0.1 mA to 0.3 mA in rodents [29] and 0.1 mA to 1 mA in humans [25]. Higher stimulation amplitudes were employed in cases of more severe injuries such as rats with crushed optic nerves (0.5 mA) or animals with larger eyes such as rabbits (0.7 mA) [30]. However, inconsistent outcomes have been reported for inducing neuroprotective effects in comparable trials. One study reported success using 0.15 mA transpalpebral stimulation in patients with dry AMD [31], an amplitude considered to be at the low-end of the spectrum in human studies [25], whereas another study using 0.8 mA amplitude and similar waveform parameters on the same disease-type did not see a statistical significance compared to the control [32]. Therefore, stimulation amplitude is not a reliable metric to characterize the setup, as the variation between the bodies of the subjects, modality (voltage- or current-controlled), quality of the stimulation system and the electrode-tissue interface will influence the electric field distribution inside the stimulated tissue. To overcome this limitation, our goal is to assess the current density generated within the targeted region, which takes the geometry and dielectric properties of the tissue into consideration. We hypothesize that it offers a more informative and encompassing metric that can ensure consistency between trials.

Here, we tested our hypothesis through a multi-scale computational method to simulate the electric fields generated in the eye during TES followed by a series of in vivo and ex vivo experiments, which are used to validate the simulation results and help characterize the electric fields produced by various setups. We empirically characterize the current-controlled stimulation amplitude required for generating the target current density in the retinas of rat and pig eyes during TES.

TABLE I
MATERIAL PROPERTIES IN THE RAT HEAD MODEL

Material Type	Resistivity (Ω.m)
Air	$1*10^{7}$
Muscle	4.82
Fat	64.6
Skin (dry)	5000
Bone	763
Brain	25.7
Sclera	1.99
Vitreous Humor	0.67
Lens	3.15
Cornea	2.4
Outer Eyelid	2456
Retina	1.5
Working Electrode	$1*10^{-7}$
Return Electrode	$1*10^{-7}$

II. METHODS

A. Computational Modeling

The modeling efforts aim to develop and leverage multi-scale computational modeling platforms to design the most efficient and safe electric stimulation configurations for minimally-invasive TES. To induce epigenetic changes and achieve the neuroprotective effect, we aim to maximize the induced current in the retina while using safe stimulation current magnitudes. With the help of our Admittance Method (AM)/NEURON multi-scale computational modeling platform, we can predict the induced electric fields inside a bulk tissue model [33]. This platform was previously used for predictive extracellular electrical stimulation in the retina [34-37] and the hippocampus [38]. Here, we leverage this method to design electrodes and their placement locations to effectively induce the electric fields in the rat and human retina during TES. We use a large-scale segmented model of a rat, including the finer structures of the eye, such as the sclera, cornea, lens, vitreous humor, and eyelid layers.

The AM can be used to modify the stimulation parameters and predict the induced voltage and current densities in the rat model. AM discretizes the model into cuboid voxels, and each voxel is represented by the lumped admittances at its edges. The admittance values are calculated using the electric properties of the tissue, which are its conductivity and permittivity. As such, the admittance values depend on the operating frequency and voxel dimensions. The 3D model is then reduced to a network of lumped admittances, a current source is applied to a given node and the induced voltage is then computed at each node of this network using iterative methods for solving a set of linear equations, computed in each axis:

$$I = GV \tag{1}$$

$$\vec{E} = \frac{V_n - V_{n+1}}{\Delta s} \tag{2}$$

$$\vec{J} = \sigma\vec{E}, \ \sigma = \frac{1}{\rho} \tag{3}$$

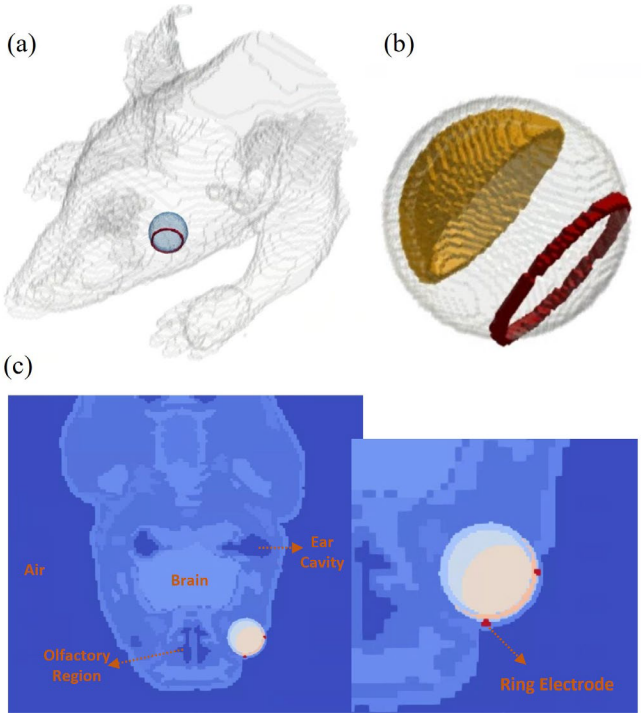

Fig. 1. (a) The 3D segmented rat model with the ring electrode (shown in red) (b) The eyeball model with retina (orange) and stimulating ring electrode (red). (c) A slice of the 3D model shows the zoomed in view of the eyeball with the surrounding structures and the ring electrode location. The front of the snout and the tissue around the eye were truncated for better visualization.

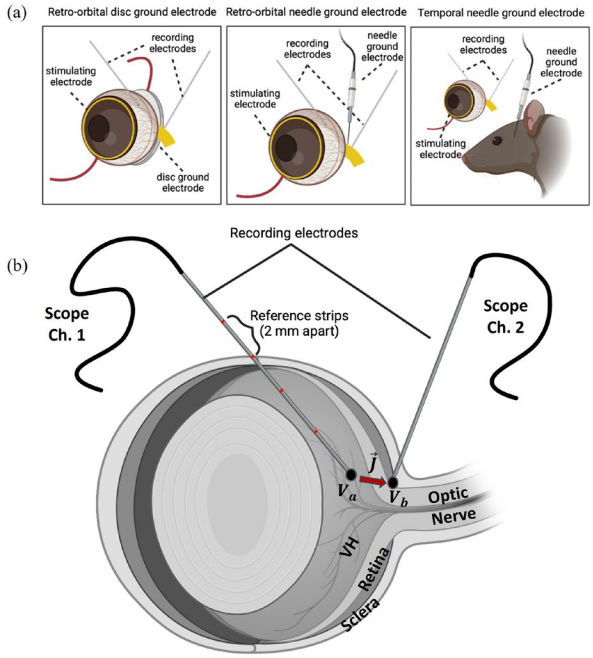

Fig. 2. (a) Schematic representation of the different TES setups with three return electrode configurations tested in vivo. (b) Illustration of the TES setup shows the two insulated W needle electrodes with exposed tips inserted in the vitreous humor and in the sclera at the base of the optic nerve to measure the voltage across the retina, at a separation of Δs = 2 mm, which is used to estimate the current density generated between them using equations (2,3). VH: Vitreous Humor

where I is a vector containing stimulation current at each node, G is the admittance matrix and V is a vector that contains induced voltage at each node. The electric field $\vec{E}$ is calculated from the voltage difference between neighboring voxels $V_n - V_{n+1}$ and their separation Δs, and the current density $\vec{J}$ is calculated using the material properties of the tissue type. A complete definition of the conductivity would include a complex term, $\sigma = \frac{1}{\rho} + j\omega\varepsilon$, signifying the frequency dependence of the displacement current in biological tissue [39]. Given the low-frequency (10-100 Hz) nature of the stimulation waveforms relevant for TES and neuroprotective approaches outlined in the introduction section, we consider a direct current (DC) approximation for this study, which simplifies the conductivity equation in (3) as $\sigma = \frac{1}{\rho}$. This approximation is valid for low-frequency problems, where the material will behave more like a conductor and the capacitive effects relating to the complex component will be minimal. A review of the bioimpedance data supports this conclusion, where the conductivity of various tissue types remains constant below 10 kHz [40]. Therefore, the mesh generated from the bulk tissue model is a network of resistors and the calculated $\vec{J}$ reflects the equivalent resistive component of the model. The resistivity of each tissue and electrode material type included in the model is summarized in Table 1. These values were obtained from the IT'IS Foundation database of tissue properties [41]. Version 4.1 of the database was available at the time of this publication. The resistivity data used here was taken from porcine tissue samples [42] and rat retina [43].

To minimize the computational cost, the 3D rat model is truncated from the sides and mostly contains the head. The truncated model is shown in Fig. 1(a) where the stimulating transcorneal ring electrode is shown in red. The retina is represented by a one voxel-thick layer, as shown in Fig. 1(b) (yellow). The eyelids are modeled using two layers: an inner eyelid layer (modeled with sclera properties) and an outer layer (modeled with wet skin properties). Fig. 1(c) shows the 2D slice of the bulk rat model, which highlights the various tissues present in the model. The resolution is 166 µm, which is the length of each side of the cuboid voxels.

B. *Electrode Connection and Stimulation Parameters*

To validate our simulation results in vivo, we designed a transcorneal electrical stimulator that could be placed on the cornea and developed a measurement technique for approximating the current density generated through the retina. A ring electrode with a 4 mm diameter was built using a 0.25 mm thick (30 AWG) pure platinum (Pt) wire, designated as the working electrode in a bipolar two-electrode setup. First return electrode was built using the same material but fashioned into a disk shape that can be placed next to the optic nerve behind the globe. Second return electrode was selected to be a monopolar 30-gauge Pt needle (F-E2-24 Subdermal Needle Electrode, Natus Medical), commonly used for subcutaneous placement in TES studies. A current pulse was delivered using a current-controlled stimulator (STG 4008, Multi Channel Systems, Harvard Bioscience, Inc.). The

stimulation waveform was a cathodic-first symmetric biphasic pulse of 1 ms phase width and 50% duty cycle for a pulse period of 4 ms. The duty cycle was maximized while making sure the inter-pulse potential during rest approached steady-state before applying the following pulse. Two tungsten (W) needle electrodes with 0.2 mm diameter (E363T/2, Protech International, Inc.) were used to pierce the eye and measure the potential difference between two points on either side of the retina, labeled as V_a and V_b (Fig. 2(b)). This potential was used to predict the current flow through the retinal layers, starting from the vitreous-ganglion cell layer border up to sclera and the root of the optic nerve. Each W electrode was connected to an individual channel of a digital storage oscilloscope (InfiniiVision DSOX2014A, Keysight Technologies) and the arithmetic difference between the channels was recorded simultaneously.

C. Animal Procedure

RCS rats were used for electrode rest optimization experiments. The care and use of the rats were conducted in accordance with the regulations and guidelines of the Institutional Animal Care and Use Committee (IACUC) of the University of Southern California (USC) which are in adherence to the National Institutes of Health (NIH) Guidelines for the Care and Use of Laboratory Animals, and the Association for Research in Vision and Ophthalmology (ARVO) Statement for the Use of Animals in Ophthalmic and Vision Research. A combination of ketamine (100mg/ml) and xylazine (100mg/ml) was administered intraperitoneally to anesthetize the animals before the procedure. Topical anesthesia such as 0.5% Tetracaine eye drops, was administered prior to any ocular manipulation.

The three different placement configurations that were tested, as illustrated in Fig. 2(a): retro-orbital disc ground electrode, retro-orbital needle ground electrode, and subcutaneous temporal needle ground electrode. Briefly, once the rat was under anesthesia, the eye, conjunctival sac, and eyelids were cleaned using a 5% povidone-iodine solution, and topical anesthesia was applied. Both superior and inferior eyelids were retracted using fine forceps. A small conjunctival incision was performed using microscissors. A conjunctival pocket was created, where the ground electrode (either disc or needle) was rested retro-orbitally. In the case of temporal placement, the ground electrode was positioned subcutaneously in front of the rat's ear. Then, one recording electrode was positioned intravitreally and one behind the orbit, piercing the sclera (Fig. 2(b)). The intravitreal electrode was inserted perpendicularly to the opposing recording electrode and pulled 2 mm apart. The separation was dictated by marking reference strips on the needle. Finally, the stimulating electrode was placed on the surface of the cornea. A clamp was used to fixate the all the electrodes in position. Grounding cuffs were attached on the rats' tails to keep the noise and offset values minimal across their body. The recordings were initiated once the time averaged shape of the waveform did not change for 60 seconds. The animals were euthanized after the experiment.

Enucleated porcine eyes were employed for further investigation of the TES parameter optimization in human studies, as their diameter is more comparable to human eyes. The porcine eyes used had a sagittal length of 24 mm on average, which necessitated the use of a Pt ring electrode with 17 mm diameter. First, any residual connective tissue was removed from the scleral surface. Like before, the recording electrodes were positioned near the optic nerve in the sclera, and intraretinally via a controlled scleral incision (Fig. 2(b)). The placement of the two recording electrodes at 2 mm separation was executed with the use of a micromanipulator in the ex vivo setup. A disc-shaped Pt return electrode was placed near the base of the optic nerve. Insulated, tip-only exposed W needle electrodes were used to measure the voltage difference inside the eye.

D. Calculation of the Current Density

The current density generated near the targeted cells is the standard metric in TES and other electrical stimulation techniques such as transcranial for inducing neuroprotective effects that promote neuronal survival. Estimation of this current density depends on the experimental setup. Using a surface area estimation will only be accurate if the geometry of the stimulated area is well defined for the surface integral calculation. Instead, we can approximate the generated current density from the electric field, which is a function of the voltage difference between two points, as described in equation (2). This equation relies on the assumptions that the generated field is electrostatic, the equivalent impedance of the bulk tissue is mostly resistive and will respond linearly to stimulation. A caveat with this approach is the sensitivity towards variations in the tissue resistivity in the target region. The resistivity even within the layers of the retina can vary significantly, from 1 to 4 Ω.m [43, 44]. Based on the electrode depth vs. resistivity analysis of the rat retina [43], we combined the values of the vitreous and retinal layers between the measuring electrodes to average out 1.5 Ω.m to use in our calculations.

III. Results

A. Simulation Results

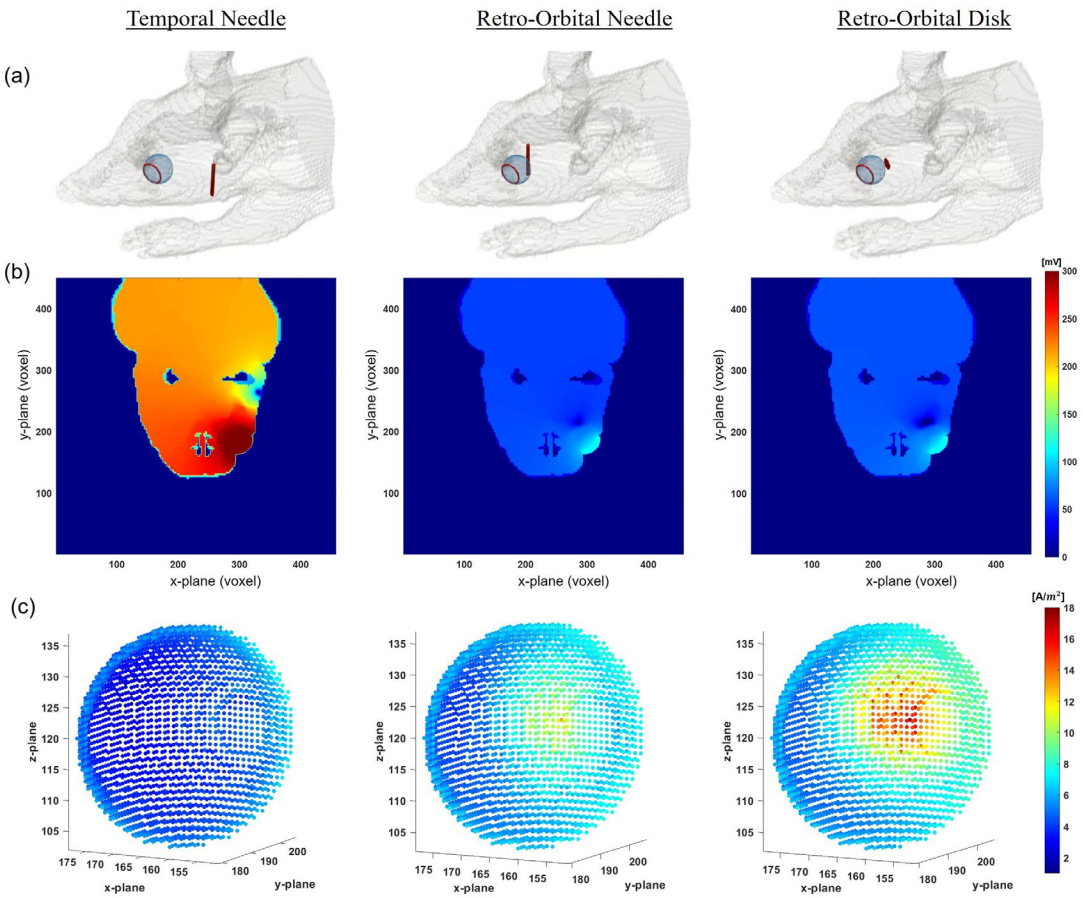

Fig. 3. Simulation results of various placements for the ground electrodes, current source placed along the ring electrode for an amplitude of 0.2 mA. Row (a): the voxelized rat head model with stimulating and return electrodes. Row (b): The voltage distribution across a 2D slice in the xy plane (passing through z = center of the stimulating ring). Row (c): the current density distribution inside the retina in the xyz plane. The left side is medial, right is lateral, top is superior and bottom is inferior direction.

Using our computational modeling approach, we evaluated the different electrode dimensions and placements. A ring electrode placed on the cornea as the working/stimulating electrode and three return electrode configurations were tested (Fig. 3(a)). The needle was a hollow cylinder with a diameter of 3 mm and a wall thickness of 0.075 mm, closest to the dimensions of a 30-gauge needle. The disc electrode diameter was set as 3 mm and thickness as 0.3 mm. The voltage mapping of the head model shows that the greatest voltage amplitude occurs when the return electrode is needle and placed subcutaneously away from the working ring (Fig. 3(b)). The electric field magnitude in the retina is related to changes in voltage (2) and both the maximum and average $\vec{J}$ were weakest when the return electrode was placed further from the target region (Table 2). The simulation results suggested that the disk ground electrode can provide higher current density at the center of the retina since the area where the current density is maximized corresponds to the electrode's spatial position (Fig. 3(c)). While placing the electrode closer to the globe is more invasive, it can provide significantly higher current in the central retina which is where the cone photoreceptors are most densely packed and the region of interest for neuroprotective effects.

Bringing the needle closer to the retina resulted in an increase both in the maximum and average $\vec{J}$ from 7.90 to 13.10 A/m^2 and 4.32 to 6.30 A/m^2, respectively and a more localized field distribution in the central regions (Fig. 3(c)). Further improvement was observed when the electrode surface was changed into a disk where the maximum $\vec{J}$ increased from 13.1 to 18.8 A/m^2 and the average $\vec{J}$ increased from 6.30 to 7.35 A/m^2, respectively. This is because a greater ratio of the electrode surface aligns with the retina layer and more of the field lines follow a direct path through the central retina into the return electrode. The disc electrode configuration yielded the highest $\vec{J}$ values and greatest control over the areas that are being stimulated, making it the ideal choice for TES.

The voltages in Fig. 3(b), the subcutaneous needle configuration, are significantly higher than the other two configurations. This happens because of the larger separation between the working and ground electrodes. As the electrode separation increases, the equivalent resistive material and the heterogeneity between the two poles increases. As a result, the electric current (field) disperses throughout the volume more, and the efficiency of charge transfer between the electrodes decreases. The charge that could not be drained dissipates, increasing the resting voltage bias of the tissue (also referred to as the "offset" voltage in this paper). It is important to have

a low offset voltage to minimize the off-target excitation in areas such as the brain and adhere to the charge injection limits that would polarizes the electrode to the onset of water redox, which could lead to tissue or electrode damage [45].

B. *In vivo and Ex vivo Experimental Results*

Following the computational analysis on the rat head model for optimizing electrode parameters in TES, in vivo experiments were performed on anesthetized rats to validate the simulation results. Three different electrode configurations at three different amplitudes were tested while recording from the same locations inside the eye (Fig. 2). The difference of the recorded potentials V_a and V_b along with the estimated separation (Δs) between them was used to calculate the electric field ($\vec{E}$) through the retina (2). The $\vec{E}$ was then multiplied with the conductivity (σ) of the rat's retina to calculate the $\vec{J}$ (3). $\vec{J}$ is the most consistent parameter used to assess the efficacy of electrical stimulation for neuroprotection and several studies have shown that the range required for inducing neuroprotective effects in transcranial stimulation is 20-50 A/m^2 [29, 46]. Aiming for these numbers in the retina, we used a TES amplitude of 200 μA, as the simulation results suggested. Amplitudes up to 400 μA were tested to determine whether $\vec{J}$ would change linearly. Because the rat's eye is much smaller than a human's and can tolerate smaller currents, the same setup was used on a pig's eye once we validated the simulation results on rats. The diameter of the pig eye is comparable to a human's, which determines how much stimulation current is needed for effective therapeutics. We aimed for a minimum of 20 A/m^2 to validate the efficacy of our stimulation protocol. According to the values obtained from the experiments and the approximations described in section 2.D, the maximum $\vec{J}$ for rat is calculated to be about 12.8 +/- 2.3 A/m^2, 14.7 +/- 4.9 A/m^2, 13.7 +/- 8.7 A/m^2 for columns 1, 2 and 3 of Fig. 4, respectively (Table 2). The range of current densities are comparable with the values computed in our simulations, which are 18.8 A/m^2 , 13.1 A/m^2, 7.9 A/m^2 for the retro-orbital disk, retro-orbital needle and temporal needle, respectively.

1) *Electrode Placement Near the Globe is More Invasive but Improves Precision*

The first trade-off that needs to be considered when optimizing TES methods is choosing the ground location in the body for placing the return electrode. Ideally, the return electrode will be minimally invasive while ensuring the threshold current density is generated in the target area. The simulations suggested that while the threshold requirement could be met whether the ground was positioned near or further from the optic nerve, the high current density areas shifted towards the periphery of the retina as the electrode was placed further away (Fig. 3(c)). To verify these results, we placed the return electrode both retro-orbitally, next to the optic nerve and temporally in the subcutaneous tissue. The mean of the maximum voltage differences measured (V_{ab}) were 39.3 mV and 47.4 mV for retro-orbital and temporal placements, respectively (Fig. 4). While the maximum V_{ab} appeared to increase as the return needle was placed further from the working ring, contrary to the simulation results in Table 2, the spread of the data was also significantly greater. The standard deviation of the measured V_{ab} were +/- 14.7 mV and +/- 26.3 mV when the needle return electrode was placed retro-orbitally and temporally respectively. Because we want to establish a correlation between the input stimulation and the $\vec{J}$ across the retina, keeping the variation to a minimum is critical for consistency across different trials. Even though the maximum $\vec{J}$ on average was smaller when the return electrode was placed closer to the globe, the confidence margin for estimating how much current is needed for inducing the target $\vec{J}$ is greater; therefore, the return electrode should be placed as close to the globe as possible for consistent results.

TABLE 2
SIMULATED AND MEASURED VALUES (I_{stim} = 200 μA, N = 10 EYES)

Variable	Subcutaneous Needle	Retro-orbital Needle	Retro-orbital Disk
$\vec{J}_{max(\text{simulated})}$ (A/m^2)	7.9	13.1	18.8
$\vec{J}_{max(\text{measured})}$ (A/m^2)	13.7	14.7	12.8
$V_{offset(simulated)}$ (mV)	215	55	60
$V_{offset(measured)}$ (mV)	78	57	24

We acknowledge a potential source of the variance between trials in the measurements shown in Fig. 4, which is due the measuring electrode positioning with respect to the axis of the optic nerve. The recorded voltages can fluctuate greatly depending on the position of the intravitreal electrode, which is especially noticeable with the needle electrodes. The simulations suggest that the percentage variation of $\vec{J}$ in the central retina can be much larger in the needle configuration (2-8 A/m^2, up to 400%) compared to the disk (8-18 A/m^2, up to 225%) depending on the coordinates of the electrode tip (Fig. 3(c)). The same pattern is apparent in Fig. 4, where the variance of the wide disk electrode is significantly smaller than the narrow needles.

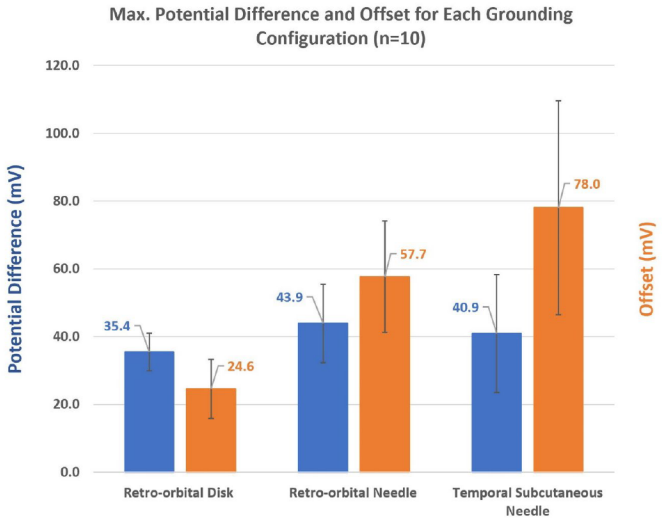

Fig. 4. The maximum voltage difference V_{ab} (blue) and the voltage offset during the inter-pulse time (orange) recorded across the 10 rats for different return electrode configurations.

2) A Large Electrode Surface Reduces the Maximum Current Density but Minimizes Off-Target Stimulation

The surface area of a stimulating electrode holds importance due to its role in the charge injection mechanism associated with double-layer formation at the electrode-tissue interface [47] and involves a trade-off between precise targeting of a small area and maintaining the charge density vs. total charge constant within the established safety threshold [48]. For our TES setup, the size of the return electrode is constrained by the physical space available around the eye for implantation and our goal is to minimize the surgical trauma. For our rat experiments, this limitation translated to a maximum diameter of 3 mm. Consequently, we opted for a disk-shaped return electrode with a 3 mm diameter and compared its performance against the retro-orbital needle electrode configuration. One important difference between the two configurations was the actual surface area that contacted the eye. One flat side of the disk (7.1 mm^2) came into contact with the globe, whereas the needle only engaged about one-third of its outer surface (3.2 mm^2). Switching from the disk to the needle electrode led to an increase in the maximum voltage from 35.4 mV to 43.9 mV on average. This increase in the maximum V_{ab} when using the needle electrode can be attributed to its higher equivalent impedance across the electrode-tissue interface. This impedance primarily arises from the smaller surface area of the needle. The current-controlled stimulator adjusts its source voltage to match the target current amplitude depending on the input impedance, which can lead to higher recorded voltage differences when using the needle electrode. However, it's important to acknowledge that the standard deviation also increased from +/- 6.9 mV to +/- 14.7 mV when transitioning from disk to needle, a trend observed when the return electrode was placed further away from the working electrode (Fig. 4). The circular shape of the disk maximized the contact area between the electrode and the eye, thereby further improving the confidence interval. This outcome suggests that the disk design remains desirable, despite a slightly smaller range of $\vec{J}$. Another important observation pertained to the voltage offset, which more than doubled on average when using the needle electrode. This increase indicated that the surrounding tissue was exposed to a higher extracellular voltage level, even when the stimulation pulse was not active. The offset value was derived by first subtracting the DC component from the recorded signals and then measuring the voltage immediately before a new pulse was applied (Fig. 5(c)). From an electrochemical perspective, a voltage offset signifies non-ideal charge transfer between the electrodes due to a mismatch in injection and discharge rates. This phenomenon can also be elucidated from a circuit perspective, where the equivalent impedance of the electrode-tissue interface is loosely modeled as a parallel RC block, often referred to as the double-layer impedance [49]. Increasing the electrode's surface area directly influences the properties of the passive elements where a greater capacitance increases the capacitive conduction through the double-layer, which is a charge injection mechanism that redistributes the charges in the electrolyte but does not involve electron transfer [47]. Consequently, this minimizes faradaic charge transfer and accumulation in the tissue, leading to a reduced voltage offset

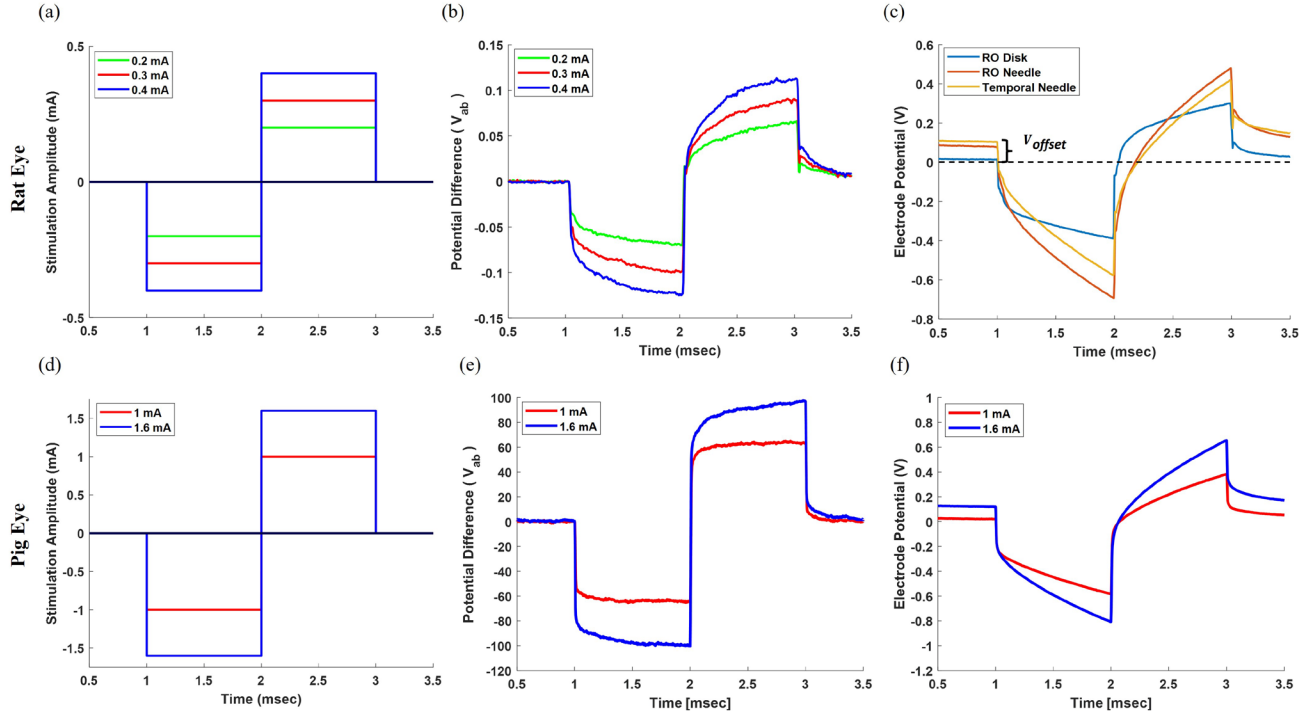

Fig. 5. Samples of waveforms recorded from rat and pig eyes. (a) Amplitudes tested on rat eyes. (b) The potential difference recorded across the rat's retina for a given amplitude. (c) The potential generated across the stimulation electrodes at an amplitude of 0.2 mA, for retro-orbital disk/needle and temporal needle configurations. The method for calculating the offset voltage during inter-pulse time is shown. (d) Amplitudes tested on pig eyes. (e) The potential difference recorded across the pig's retina for a given amplitude. (f) The potential generated across the disk stimulation electrode at a given amplitude. The voltage offset becomes non-zero beyond 1 mA amplitude, which may be a limiting factor in terms of stimulation safety.

during resting periods. Given the imperative to avoid off-target excitation in TES, it is important to have a sufficiently large electrode to minimize the voltage offset generated in the surrounding areas, while ensuring that the charge density remains at a safe level. Once again, the advantage of using a disk-shaped electrode is emphasized as its geometry aids in maximizing the covered surface area.

3) Pig's Eye Requires 1 mA Stimulation to Reach 20 A/m^2 Current Density

After successfully validating the simulation results of the rat's eye through in vivo recordings, we applied the same experimental setup to the pig's eye to estimate the required stimulation amplitude for achieving a minimum current density of 20 A/m^2 in its retina. The stimulation amplitude required to elicit the target $\vec{J}$ depends on the tissue volume between the electrodes and its equivalent impedance. We selected the pig's eye for this study due to its similarity in volume to a human eye. To accommodate a higher charge per phase and maintain charge density, we employed a larger disk return electrode with a 6 mm diameter on the pig's eye, in contrast to the setup used for rats (3 mm). Like before, we recorded voltages simultaneously across the two electrodes separated by 2 mm and plotted the differences using an oscilloscope (Fig. 5(e)). Notably, a stimulation amplitude of 1 mA resulted in a V_{ab} of up to 60 mV across all four eyes tested, with an average of 56 mV and a standard deviation of +/- 4.2 mV. Assuming an average combined tissue resistivity of 1.5 Ω.m through the VH and the retina, we can approximate that the generated current density was approximately 20 A/m^2. Similar to our observations in rat experiments, increasing the stimulation amplitude yielded a roughly linear scaling in the V_{ab}, where a 60% increase in amplitude (1 mA to 1.6 mA) led to a 53% increase (from 60 mV to 92 mV). As the equipment limit was 1.6 mA, higher stimulation amplitudes could not be tested. These findings can be extrapolated to the adult human eye, which is slightly larger than the pig eye. Consequently, our results suggest that a minimum amplitude of 1 mA should be considered for use in TES trials on human subjects.

4) Current Density Scales Linearly with Stimulation Amplitude

In the equivalent circuit model of an electrochemical system, the tissue component (electrolyte) is typically considered as a purely resistive series load. Assuming that the reactive component of the electrode impedance cancels out when subtracting one potential from another (V_{ab}), the equivalent load between the electrodes can be represented by a resistor. Consequently, we hypothesized that the current vs. voltage relationship must be linear adhering to Ohm's law. To test this hypothesis, we conducted experiments at three different stimulation amplitudes: 0.2 mA, 0.3 mA, and 0.4 mA for rat (Fig. 5(a)), and plotted the resulting voltage differences (Fig. 5(b)). The increase in the V_{ab} closely followed that of the stimulation amplitude during the rat experiments, where gains of 44% and 24.5% in the V_{ab} were measured for 50% and 33.3% increase in the amplitude, respectively. Similarly, experiments conducted on the pig's eye showed a 53% increase (from 60 to 92 mV) when stimulated with 60% more current (1 mA to 1.6 mA) (Fig. 5(e)). Both the transitions observed in rat from 0.2 mA to 0.3 mA and in pig from 1 mA to 1.6 mA led to a gain in V_{ab} vs. amplitude increase ratio of 88%, whereas it was 73% in the case of rat going from 0.3 mA to 0.4 mA. These findings suggest the possibility of diminishing returns with respect to increasing the stimulation amplitude concerning the $\vec{J}$ generated in the target area. A plausible explanation for this pattern lies in the dynamics of charge transfer at the electrode-electrolyte interface, the equivalent circuit model of which has complex components [47]. This includes a capacitor realistically modeled as a constant phase element, which is non-ideal and adds amplitude and frequency dependency to the equivalent capacitance. A changing capacitance value due to the non-ideal dynamics may ultimately lead to a nonlinear input/output relationship.

5) Current Density Does Not Reach the Contralateral Eye

An important consideration in TES is ensuring that the induced current density remains isolated within the target area and does not interfere with the stimulation of the contralateral eye. To assess how far the induced current density extends from the return electrode, we took voltage difference measurements across the stimulated target eye, between the two eyes and across the contralateral eye (Fig. 6, top row). A V_{ab} up to 100 mV was measured across the stimulated right eye, consistent with the results from previous trials illustrated in Fig. 4. However, as the measuring electrodes were shifted away from the right eye, the V_{ab} dropped substantially to about 10 mV at the midpoint between the left and right eyes. When the measurement was taken across the left eye, the V_{ab} registered as zero, indicating that the $\vec{J}$ near the left eye was

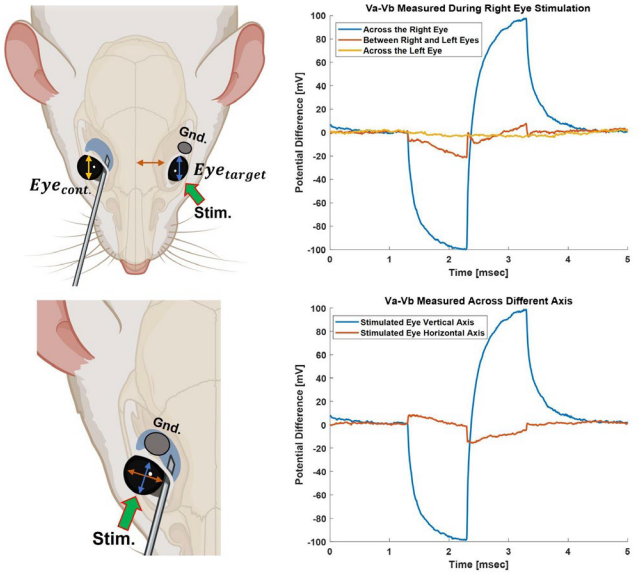

Fig. 6. (Top Row) The TES was set up on the right eye while the voltage difference was measured across the sclera of the right eye (blue arrow), halfway between the two eyes (orange arrow) and across the sclera of the left eye (yellow arrow). The V_{ab} approaches zero sharply moving away from the right eye, indicating that the current density generated outside the target area is negligible. (Bottom Row) The V_{ab} was measured across the perpendicular axes to determine the directionality of the electric field generated in the eye tissue. The vertical V_{ab} between the cornea and the optic nerve was significantly higher than the horizontal V_{ab} between medial and lateral sides, indicating that the induced fields cross the retina perpendicularly.

negligible during the stimulation of the right eye. In a related test, we measured the V_{ab} along two axes relative to the orientation of the ring electrode. The vertical contour extended from one electrode to the other, while the horizontal contour ran perpendicular to the vertical contour, equidistant from either electrode (Fig. 6, bottom row). The V_{ab} measurements along these contours revealed that the electric field lines predominantly followed a direct vertical path between the working and return electrodes, thereby generating a stronger $\vec{J}$ across the thickness of the retina from the ganglion cell layer towards the photoreceptor layer. This observation aligned with the simulations demonstrated in Fig. 3(c), where the $\vec{J}$ was most pronounced in the center for the disk electrode and decreased sharply as it approached the peripheral regions. However, we note that there remained a non-zero difference both in the simulations and the experimental measurements. This discrepancy can be attributed to the placement of the return electrode, which was located towards the left side of the optic nerve and featured a large diameter extending towards the periphery. This pattern suggests that one half of the retina receives a stronger stimulation with the disk return electrode design employed in our study.

IV. Discussion

Characterizing the current density generated in the retina during TES is crucial for optimizing its effectiveness in promoting neuroprotection in the targeted area. Previous experiments on various neural cells have shown that a minimum current density is necessary to induce neuroprotective effects and support cell survival [19, 29]. To ensure the consistency of stimulation trials, it's essential to establish a relationship between the input amplitude and the current density $\vec{J}$ in the retina. Towards this goal, we developed a computational model for the rat's head using the Admittance Method technique, developed by our group. We simulated various return electrode configurations for TES in terms of placement location and geometry to optimize the distribution and amplitude of $\vec{J}$ in the retina. The simulation results suggested that an invasive approach using a large-surface disk return electrode near the globe was significantly more effective in generating a greater $\vec{J}$ at the retina. Importantly, the flat disk provided greater control over the area of activation, making the disk return electrode positioned on the globe superior to the other configurations for TES (Fig. 3(c)). Although more invasive, return electrode implantation behind the globe might be a necessary trade-off to achieve effective therapeutics and neuroprotection in the retina. Considering the mixed TES clinical trial outcomes for preserving visual functions of RP patients, the necessity of an optimized stimulation approach is clear. A skin patch return electrode setup was used in the studies outlined in the Introduction section, which would be closest to our temporal subcutaneous needle configuration. The simulations suggested that the temporal placement generated the weakest $\vec{J}$ at the retina while the in vivo data suggested it had the highest variance. The retro-orbital disk was superior in both aspects with the highest simulated $\vec{J}$, lowest simulated/measured offset voltage, and lowest variance in measurements (Figs. 3,4, Table 2). One similar computational study on TES for DTL electrodes (human) has reported that an electric field of 1 mV/mm in the retina can be generated at a stimulation amplitude of 62 μA [50]. Our ex vivo measurements on pig's eye using the disk electrode configuration demonstrated an electric field of (58 mV) / (2 mm) at an amplitude of 1000 μA, scaled to 1.8 mV/mm at 62 μA with linear approximation (Fig. 5(e)). This difference further reinforces the advantage of placing the return electrode closer to the retina for maximum efficacy. Our results contribute towards the optimization of return electrode design for a consistent $\vec{J}$ to ensure an effective neuroprotective stimulation protocol. It is noted that a new implantation protocol would be needed for translation of the proposed design to the clinical arena.

The experimental data corroborated the simulation results and served to validate our computational methods. On average, the measured $\vec{J}$ in rats was 33% smaller than the simulations, which can be expected considering the imperfections of a real system, variation among animals and limited accuracy of the measuring electrodes. We acknowledge that the most significant source of error in estimating the $\vec{J}$ using equation (2) likely stems from differences in model and actual tissue conductivities. As we could not accurately measure the voltage difference across the individual layers of the retina, resistivity of which can vary significantly, we relied on a combined resistivity value of the retina and the vitreous humor obtained from the literature to calculate $\vec{J}$. The large 200 μm diameter needle measuring probe posed another limitation, as the thickness of the different retinal layers in the RCS rat ranges from 40 μm to 100 μm [51]. Ideally, a high-resolution microelectrode probe, similar to the one used by Kasi et al. [43], would be able to measure the voltage differences within a 10 μm thickness, sufficient for accurate characterization of current density within individual retinal layers during TES. Further, we acknowledge the error stemming from the positioning of the two measuring electrodes, discussed in section 3.B.1, leading to a large variance in the recorded $\vec{J}$ between trials. Therefore, the experimental values reported in this paper should largely be considered supportive of our simulation results of the $\vec{J}$ generated in the retina.

Overall, the data collected from the rats demonstrated the reliability of our computational model as a predictor of fields generated in the eye during TES and helped establish an input/output relationship for a current-controlled stimulator. The values obtained from rat's eyes suggest a minimum stimulation amplitude of 0.2-0.3 mA whereas those obtained from pig's eyes suggest a minimum of 1 mA for reliably generating the target $\vec{J}$ of 20 A/m^2 in the retina. Data from pig eyes are more relevant for translation into human studies, given their comparable dimensions. The determined threshold current amplitude from our data falls within the range of TES human trials that have successfully slowed down vision loss in

patients with retinitis pigmentosa, who received stimulation ranging from 0.8 to 1 mA [25]. Nevertheless, there is a practical limit to the current amplitude that can be comfortably delivered in conscious subjects. In our experiments with rats under anesthesia, we observed extraocular muscle twitching and facial spasms in some cases when exceeding 0.3 mA. As the stimulation amplitude cannot be increased freely until the target $\vec{J}$ is reached due to tolerance limits, optimizing electrode design remains an important component in achieving successful outcomes in TES.

Other computational work involving different tissue types using the AM has demonstrated the potential to generate results that can be experimentally validated. Predictive simulations of the local field potential (LFP) generated in the hippocampus due to extracellular electrical stimulation was successfully validated through analytically estimated LFPs [38]. Additionally, the neuronal response of two retinal ganglion cell subtypes with different frequency responses during epiretinal stimulation was accurately simulated by combining the AM with the NEURON computational platform to predict the mechanisms of color encoding [52]. Most recently, the TES approach was evaluated in tandem with the retina model of rat and AM-NEURON computational platform to design stimulation strategies for targeting the bipolar cell and photoreceptor layers affected during early-stage degeneration [53]. These computational studies have demonstrated that AM can reliably be used for predictive analysis on induced fields and neuronal activation in electrophysiology applications. Our future efforts will focus on developing a realistic human head model and simulating the activation of specific cell subtypes in the retina during TES using the AM-NEURON computational platform, leveraging the stimulation parameters optimized in this study. Understanding how different retinal cells respond to extracellular potentials generated with TES will be crucial for developing therapeutic strategies, such as targeted activation of specific subtypes.

V. Conclusion

We have developed an innovative multi-scale computational method aimed at analyzing the response of a comprehensive mouse head model to transcorneal electrical stimulation (TES) for therapeutic applications. Our model compared stimulation thresholds for various electrode placements, providing valuable insights into the optimal design and placement of the return electrode to maximize current density in the retina. Notably, the simulation results aligned closely with the experimental data collected in vivo from rats. The comparison between simulated and measured voltage and current density values demonstrated that employing the Admittance Method for modeling bioelectromagnetic interactions during TES is a dependable approach for optimization and predictive analysis. This computational tool assumes even greater importance in the context of human trials, where direct invasive measurements are not feasible, and modeling studies become essential for predicting current densities generated in biological tissue. Future validation studies should prioritize in vivo recordings from species with eye sizes comparable to those of humans, as live body recordings may yield different results compared to studies conducted on severed tissue. Once validated, computational models, such as the one presented here, can be leveraged to optimize the stimulation parameters in electrophysiology applications, thereby enhancing the success rate of neuroprotective and regenerative therapies.

References

[1] C. Hamel, "Retinitis pigmentosa," *Orphanet journal of rare diseases,* vol. 1, no. 1, pp. 1-12, 2006.

[2] A. L. Wang, D. K. Knight, T. V. Thanh-thao, and M. C. Mehta, "Retinitis pigmentosa: review of current treatment," *International ophthalmology clinics,* vol. 59, no. 1, pp. 263-280, 2019.

[3] Q. Zhang, "Retinitis pigmentosa: progress and perspective," *The Asia-Pacific Journal of Ophthalmology,* vol. 5, no. 4, pp. 265-271, 2016.

[4] J. R. Mendell *et al.*, "Current clinical applications of in vivo gene therapy with AAVs," *Molecular Therapy,* vol. 29, no. 2, pp. 464-488, 2021.

[5] J. Hanus, F. Zhao, and S. Wang, "Current therapeutic developments in atrophic age-related macular degeneration," *British Journal of Ophthalmology,* vol. 100, no. 1, pp. 122-127, 2016.

[6] A. H. Kashani *et al.*, "Survival of an HLA-mismatched, bioengineered RPE implant in dry age-related macular degeneration," *Stem Cell Reports,* vol. 17, no. 3, pp. 448-458, 2022.

[7] A. H. Kashani *et al.*, "A bioengineered retinal pigment epithelial monolayer for advanced, dry age-related macular degeneration," *Science Translational Medicine,* vol. 10, no. 435, p. eaao4097, 2018.

[8] L. Yue, V. Wuyyuru, A. Gonzalez-Calle, J. D. Dorn, and M. S. Humayun, "Retina–electrode interface properties and vision restoration by two generations of retinal prostheses in one patient—one in each eye," *Journal of Neural Engineering,* vol. 17, no. 2, p. 026020, 2020.

[9] K. Chang, S. Enayati, K.-S. Cho, T. P. Utheim, and D. F. Chen, "Non-invasive electrical stimulation as a potential treatment for retinal degenerative diseases," *Neural Regeneration Research,* vol. 16, no. 8, pp. 1558-1559, 2021.

[10] S. K. Agadagba, L. W. Lim, and L. L. H. Chan, "Advances in transcorneal electrical stimulation: from the eye to the brain," *Frontiers in Cellular Neuroscience,* vol. 17, p. 1134857, 2023.

[11] M. Hu *et al.*, "Electrical stimulation enhances neuronal cell activity mediated by Schwann cell derived exosomes," *Scientific reports,* vol. 9, no. 1, p. 4206, 2019.

[12] S. Enayati *et al.*, "Electrical stimulation induces retinal Müller cell proliferation and their progenitor cell potential," *Cells,* vol. 9, no. 3, p. 781, 2020.

[13] Y.-q. Ni, D.-k. Gan, H.-d. Xu, and G.-z. Xu, "Neuroprotective effect of transcorneal electrical stimulation on light-induced photoreceptor degeneration," *Experimental neurology,* vol. 219, no. 2, pp. 439-452, 2009.

[14] A. Schatz *et al.*, "Transcorneal electrical stimulation shows neuroprotective effects in retinas of light-exposed rats," *Investigative Ophthalmology & Visual Science,* vol. 53, no. 9, pp. 5552-5561, 2012.

[15] H. Yu *et al.*, "Noninvasive electrical stimulation improves photoreceptor survival and retinal function in mice with inherited photoreceptor degeneration," *Investigative Ophthalmology & Visual Science,* vol. 61, no. 4, pp. 5-5, 2020.

[16] T. Morimoto, T. Miyoshi, S. Matsuda, Y. Tano, T. Fujikado, and Y. Fukuda, "Transcorneal electrical stimulation rescues axotomized retinal ganglion cells by activating endogenous retinal IGF-1 system," *Investigative ophthalmology & visual science,* vol. 46, no. 6, pp. 2147-2155, 2005.

[17] P. Henrich-Noack, N. Voigt, S. Prilloff, A. Fedorov, and B. A. Sabel, "Transcorneal electrical stimulation alters morphology and survival of retinal ganglion cells after optic nerve damage," *Neuroscience Letters,* vol. 543, pp. 1-6, 2013.

[18] H. Yin *et al.*, "Transcorneal electrical stimulation promotes survival of retinal ganglion cells after optic nerve transection in rats accompanied by reduced microglial activation and TNF-α expression," *Brain Research,* vol. 1650, pp. 10-20, 2016.

[19] T. Morimoto *et al.*, "Transcorneal electrical stimulation promotes the survival of photoreceptors and preserves retinal function in royal college of surgeons rats," *Investigative ophthalmology & visual science,* vol. 48, no. 10, pp. 4725-4732, 2007.

[20] P. Henrich-Noack, E. G. Sergeeva, and B. A. Sabel, "Non-invasive electrical brain stimulation: from acute to late-stage treatment of central nervous system damage," *Neural Regeneration Research,* vol. 12, no. 10, p. 1590, 2017.

[21] K.-i. Miyake, M. Yoshida, Y. Inoue, and Y. Hata, "Neuroprotective effect of transcorneal electrical stimulation on the acute phase of optic nerve injury," *Investigative ophthalmology & visual science,* vol. 48, no. 5, pp. 2356-2361, 2007.

[22] A. K. Bittner and K. Seger, "Longevity of visual improvements following transcorneal electrical stimulation and efficacy of retreatment in three individuals with retinitis pigmentosa," *Graefe's Archive for Clinical and Experimental Ophthalmology,* vol. 256, pp. 299-306, 2018.

[23] G. Miura *et al.*, "Clinical trial to evaluate safety and efficacy of transdermal electrical stimulation on visual functions of patients with retinitis pigmentosa," *Scientific reports,* vol. 9, no. 1, p. 11668, 2019.

[24] A. Schatz *et al.*, "Transcorneal electrical stimulation for patients with retinitis pigmentosa: a prospective, randomized, sham-controlled exploratory study," *Investigative ophthalmology & visual science,* vol. 52, no. 7, pp. 4485-4496, 2011.

[25] A. Stett, A. Schatz, F. Gekeler, and J. Franklin, "Transcorneal electrical stimulation dose-dependently slows the visual field loss in retinitis pigmentosa," *Translational Vision Science & Technology,* vol. 12, no. 2, pp. 29-29, 2023.

[26] J. K. Jolly *et al.*, "Transcorneal electrical stimulation for the treatment of retinitis pigmentosa: a multicenter safety study of the OkuStim® system (TESOLA-study)," *Ophthalmic research,* vol. 63, no. 3, pp. 234-243, 2020.

[27] S. K. Wagner *et al.*, "Transcorneal electrical stimulation for the treatment of retinitis pigmentosa: results from the TESOLAUK trial," *BMJ Open Ophthalmology,* vol. 2, no. 1, p. e000096, 2017.

[28] M. della Volpe-Waizel, H. C. Zuche, U. Müller, A. Rickmann, H. P. Scholl, and M. G. Todorova, "Metabolic monitoring of transcorneal electrical stimulation in retinitis pigmentosa," *Graefe's Archive for Clinical and Experimental Ophthalmology,* vol. 258, pp. 79-87, 2020.

[29] W.-S. Yu, S.-H. Kwon, S. K. Agadagba, L.-L.-H. Chan, K.-H. Wong, and L.-W. Lim, "Neuroprotective effects and therapeutic potential of transcorneal electrical stimulation for depression," *Cells,* vol. 10, no. 9, p. 2492, 2021.

[30] M. T. Pardue, V. T. Ciavatta, and J. R. Hetling, "Neuroprotective effects of low level electrical stimulation therapy on retinal degeneration," *Retinal Degenerative Diseases: Mechanisms and Experimental Therapy,* pp. 845-851, 2014.

[31] L. Chaikin, K. Kashiwa, M. Bennet, G. Papastergiou, and W. Gregory, "Microcurrent stimulation in the treatment of dry and wet macular degeneration," *Clinical ophthalmology,* pp. 2345-2353, 2015.

[32] K. Shinoda *et al.*, "Transcutaneous electrical retinal stimulation therapy for age-related macular degeneration," *The Open Ophthalmology Journal,* vol. 2, p. 132, 2008.

[33] C. J. Cela, "A multiresolution admittance method for large-scale bioelectromagnetic interactions," North Carolina State University, 2010.

[34] J. Paknahad, P. Kosta, J.-M. C. Bouteiller, M. S. Humayun, and G. Lazzi, "The sensitivity of retinal bipolar cells response to long stimulus pulse durations in epiretinal prostheses," *Investigative ophthalmology & visual science,* vol. 62, no. 8, pp. 3169-3169, 2021.

[35] K. Loizos, "A MULTISCALE COMPUTATIONAL MODELING PLATFORM FOR DESIGN AND ANALYSIS OF ELECTRICAL NEURAL STIMULATION," The University of Utah, 2017.

[36] K. Loizos, R. Marc, M. Humayun, J. R. Anderson, B. W. Jones, and G. Lazzi, "Increasing electrical stimulation efficacy in degenerated retina: stimulus waveform design in a multiscale computational model," *IEEE Transactions on Neural Systems and Rehabilitation Engineering,* vol. 26, no. 6, pp. 1111-1120, 2018.

[37] J. Paknahad, M. Humayun, and G. Lazzi, "Selective activation of retinal ganglion cell subtypes through targeted electrical stimulation parameters," *IEEE Transactions on Neural Systems and Rehabilitation Engineering,* vol. 30, pp. 350-359, 2022.

[38] C. S. Bingham *et al.*, "Admittance method for estimating local field potentials generated in a multi-scale neuron model of the hippocampus," *Frontiers in computational neuroscience,* p. 72, 2020.

[39] D. Miklavčič, N. Pavšelj, and F. X. Hart, "Electric properties of tissues," *Wiley encyclopedia of biomedical engineering,* 2006.

[40] C. Gabriel, A. Peyman, and E. H. Grant, "Electrical conductivity of tissue at frequencies below 1 MHz," *Physics in medicine & biology,* vol. 54, no. 16, p. 4863, 2009.

[41] D. G. F. Hasgall PA, Baumgartner C, Neufeld E, Lloyd B, Gosselin MC, Payne D, Klingenböck A, Kuster N. "IT'IS Database for thermal and electromagnetic parameters of biological tissues." (accessed.

[42] S. Gabriel, R. Lau, and C. Gabriel, "The dielectric properties of biological tissues: III. Parametric models for the dielectric spectrum of tissues," *Physics in medicine & biology,* vol. 41, no. 11, p. 2271, 1996.

[43] H. Kasi, R. Meissner, A. Babalian, H. Van Lintel, A. Bertsch, and P. Renaud, "Direct localised measurement of electrical resistivity profile in rat and embryonic chick retinas using a microprobe," *Journal of Electrical Bioimpedance,* vol. 1, no. 1, pp. 84-92, 2011.

[44] B. Wang and J. D. Weiland, "Resistivity profiles of wild-type, rd1, and rd10 mouse retina," in *2015 37th Annual International Conference of the IEEE Engineering in Medicine and Biology Society (EMBC)*, 2015: IEEE, pp. 1650-1653.

[45] S. F. Cogan, K. A. Ludwig, C. G. Welle, and P. Takmakov, "Tissue damage thresholds during therapeutic electrical stimulation," *Journal of neural engineering,* vol. 13, no. 2, p. 021001, 2016.

[46] J. Huang and K. Zhao, "Neuroprotection by transcranial direct current stimulation in rodent models of focal ischemic stroke: a meta-analysis," *Frontiers in Neuroscience,* vol. 15, p. 761971, 2021.

[47] D. R. Merrill, M. Bikson, and J. G. Jefferys, "Electrical stimulation of excitable tissue: design of efficacious and safe protocols," *Journal of neuroscience methods,* vol. 141, no. 2, pp. 171-198, 2005.

[48] R. V. Shannon, "A model of safe levels for electrical stimulation," *IEEE Transactions on biomedical engineering,* vol. 39, no. 4, pp. 424-426, 1992.

[49] A. Groß and S. Sakong, "Modelling the electric double layer at electrode/electrolyte interfaces," *Current Opinion in Electrochemistry,* vol. 14, pp. 1-6, 2019.

[50] Z. Lu *et al.*, "An in-silico analysis of retinal electric field distribution induced by different electrode design of trans-corneal electrical stimulation," *Journal of Neural Engineering,* vol. 19, no. 5, p. 055004, 2022.

[51] 安達功武, "Optical coherence tomography of retinal degeneration in Royal College of Surgeons rats and its correlation with morphology and electroretinography," 2017.

[52] J. Paknahad, K. Loizos, L. Yue, M. S. Humayun, and G. Lazzi, "Color and cellular selectivity of retinal ganglion cell subtypes through frequency modulation of electrical stimulation," *Scientific reports,* vol. 11, no. 1, p. 5177, 2021.

[53] A. Gonzalez Calle *et al.*, "An extraocular electrical stimulation approach to slow down the progression of retinal degeneration in an animal model," *Scientific Reports,* vol. 13, no. 1, p. 15924, 2023.